

See discussions, stats, and author profiles for this publication at: <https://www.researchgate.net/publication/6341474>

Excited State Intramolecular Proton Transfer in 2-(2'-Arylsulfonamidophenyl)benzimidazole Derivatives: Insights into the Origin of Donor Substituent-Induced Emission Energy Shifts

ARTICLE in THE JOURNAL OF PHYSICAL CHEMISTRY A · JUNE 2007

Impact Factor: 2.69 · DOI: 10.1021/jp068832s · Source: PubMed

CITATIONS

26

READS

66

6 AUTHORS, INCLUDING:



Maged Henary

Georgia State University

94 PUBLICATIONS 1,483 CITATIONS

SEE PROFILE



Christoph J Fahrni

Georgia Institute of Technology

49 PUBLICATIONS 3,257 CITATIONS

SEE PROFILE

Excited State Intramolecular Proton Transfer in 2-(2'-Arylsulfonamidophenyl)benzimidazole Derivatives: Insights into the Origin of Donor Substituent-Induced Emission Energy Shifts

Yonggang Wu, PaDreyia V. Lawson, Maged M. Henary, Karin Schmidt, Jean-Luc Brédas, and Christoph J. Fahrni*

School of Chemistry and Biochemistry and Petit Institute for Bioengineering and Bioscience, Georgia Institute of Technology, 901 Atlantic Drive, Atlanta, Georgia 30332-0400

Received: December 21, 2006; In Final Form: March 13, 2007

Donor-substituted 2-(2'-arylsulfonamidophenyl)benzimidazoles undergo efficient excited-state intramolecular proton transfer (ESIPT) upon photoexcitation. The tautomer emission energy depends strongly on the substituent attachment position on the fluorophore π -system. While substitution with a donor group in the *para*-position relative to the sulfonamide moiety yields an emission energy that is red-shifted relative to the unsubstituted fluorophore, fluorescence of the *meta*-substituted derivative appears blue-shifted. To elucidate the origin of the surprisingly divergent emission shifts, we performed detailed photophysical and quantum chemical studies with a series of methoxy- and pyrrole-substituted derivatives. The nature and contribution of solvent–solute interactions on the emission properties were analyzed on the basis of solvatochromic shift data using Onsager's reaction field model, Reichardt's empirical solvent polarity scale $E_T(30)$, as well as Kamlet–Abboud–Taft's empirical solvent index. The studies revealed that all ESIPT tautomers emit from a moderately polarized excited-state whose dipole moment is not strongly influenced by the donor-attachment position. Furthermore, the negative solvatochromic shift behavior was most pronounced in protic solvents presumably due to specific hydrogen-bonding interactions. The extrapolated gas-phase emission energies correlated qualitatively well with the trends in Stokes shifts, suggesting that solute–solvent interactions do not play a significant role in explaining the divergent emission energy shifts. Detailed quantum chemical calculations not only confirmed the moderately polarized nature of the ESIPT tautomers but also provided a rationale for the observed emission shifts based on the differential change in the HOMO and LUMO energies. The results gained from this study should provide guidelines for tuning the emission properties of this class of ESIPT fluorophores with potential applications in analytical chemistry, biochemistry, or materials science.

Introduction

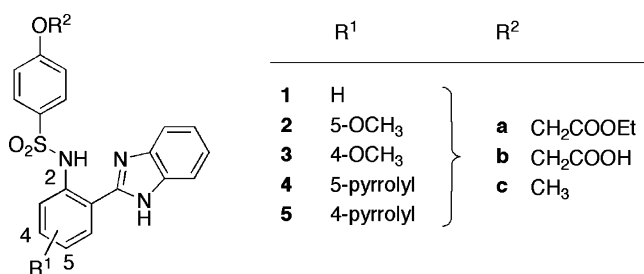
Excited-state intramolecular proton transfer (ESIPT) represents an intriguing photophysical process that can be exploited for the design of fluorescent labels^{1–3} and probes for sensing changes in pH,⁴ membrane potential,^{5–7} lipid bilayer structure,^{8,9} electric field,¹⁰ local hydration,^{11,12} temperature,¹³ as well as anion¹⁴ and metal cation^{4,15–23} concentrations. Fluorophores that undergo ESIPT are typically composed of a proton donor and acceptor connected through an intramolecular hydrogen bond. Upon photoexcitation, the proton moves toward the acceptor moiety, thus generating a phototautomer that fluoresces with an unusually large Stokes shift at lower energy. Although numerous studies have been devoted to understanding fundamental aspects of the ESIPT process, most of the work focused on unsubstituted fluorophore platforms.^{24–29} Recent studies demonstrated that the peak emission energies of the ESIPT phototautomer of substituted 2-(2'-arylsulfonamidophenyl)-benzimidazoles³⁰ and 2-(2'-hydroxyphenyl)benzazoles³¹ depend not only on the nature of the substituent but also on its attachment position on the fluorophore π -system. Variation of the latter revealed a surprisingly divergent shift of the respective emission energies. For example, compound **2** containing a methoxy group in the *para*-position relative to the sulfonamide

moiety displayed a peak emission energy that is red-shifted relative to the unsubstituted parent fluorophore **1**, while emission of the *meta*-substituted derivative **3** appeared blue-shifted (Chart 1).³⁰

Understanding of the origin of the observed emission shifts in relation to the substituent attachment position is key for the rational design of ESIPT fluorophores with tailored photophysical properties. In principle, the divergent shifts might be caused by differences in excited-state polarization that would be particularly pronounced in polar solvents such as water through isotropic solute–solvent interactions. Alternatively, differences in the strengths of the intramolecular hydrogen bond might influence the excited-state energetics and extent of geometrical reorganization in the course of the proton-transfer process, thus resulting in substantially different Stokes shifts. Finally, it would be also conceivable that the energy of the frontier orbitals involved in fluorescence emission might be differentially affected by the attachment position of the substituent. To evaluate the contribution of each of these effects and thus to elucidate the true nature of the divergent phototautomer emission shifts of *para*- vs *meta*-substituted 2-(2'-arylsulfonamidophenyl)-benzimidazoles, we decided to perform detailed photophysical and quantum chemical analyses of the *para*- and *meta*-substituted methoxy-derivatives **2** and **3** as a case study. In addition, we utilized the pyrrole derivatives **4** and **5** to explore whether hydrogen-bonding interactions with the methoxy oxy-

* To whom correspondence should be addressed: Telephone: 404-385-1164/fax: 404-894-2295. E-mail: fahrni@chemistry.gatech.edu.

CHART 1



gen lone-pair electrons are important for the photophysical properties of **2** and **3** in protic solvents.

Experimental Section

Synthesis. Fluorophores **1a/b**, **2a/b**, and **3a/b** were synthesized following published procedures.^{16,30} NMR: δ in ppm vs SiMe₄ (0 ppm, ¹H, 400 MHz), br = exchange broadened signal. MS: selected peaks; *m/z*. Melting points are uncorrected. Flash chromatography (FC): Merck silica gel (240–400 mesh). TLC: 0.25 mm, Merck silica gel 60 F₂₅₄, visualizing at 254 nm or with 2% KMnO₄ solution.

a. 2-Nitro-5-pyrrol-1-yl-benzaldehyde (8). In a Schlenk tube 2-nitro-5-bromobenzaldehyde³² (**6**, 500 mg, 2.17 mmol), freshly distilled pyrrole (133 mg, 1.97 mmol, 0.137 mL), palladium acetate (4.4 mg, 0.02 mmol), xantphos (34 mg, 0.059 mmol), and potassium carbonate (817 mg, 5.91 mmol) were mixed in 5 mL of *o*-xylene. The mixture was degassed and the tube refilled with argon. After heating at 120 °C overnight, the mixture was cooled to room temperature, washed with water, and extracted with EtOAc. The combined organic extracts were dried over anhydrous MgSO₄ and concentrated under reduced pressure. The residue was purified on silica gel (FC, EtOAc–hexanes, 2:9) providing 367 mg (1.7 mmol, 78% yield) of **8** as a yellow solid: mp 74–76 °C. *R*_f 0.47 (EtOAc–hexanes, 2:9); ¹H NMR (CDCl₃, 400 MHz) δ 6.46 (t, *J* = 2.2 Hz, 2H), 7.22 (t, *J* = 2.2 Hz, 2H), 7.69 (dd, *J* = 8.9, 2.6 Hz, 1H), 7.89 (d, *J* = 2.6 Hz, 1H), 8.27 (d, *J* = 8.9 Hz, 1H), 10.53 (s, 1H); MS (70 eV) *m/z* 216 ([*M*⁺], 100), 186 (31), 158.1 (23), 141.1 (52), 130 (30), 115.1 (38); EI–HRMS calculated for [*M*⁺] C₁₁H₈N₂O₃ 216.05349, found 216.05407.

b. 2-(2-Nitro-5-pyrrol-1-yl-phenyl)-1H-benzimidazole (10). A mixture of aldehyde **8** (200 mg, 0.925 mmol), *o*-phenylenediamine (120 mg, 1.11 mmol), acetic acid (0.08 mL, 1.4 mmol), and copper(II) acetate monohydrate (183 mg, 0.92 mmol) in 20 mL of ethanol–water (1:1) was refluxed overnight. The reaction mixture was cooled to room temperature and quenched by addition of 10 mL of concentrated aqueous NH₄OH. The mixture was extracted with EtOAc, and the combined organic extracts were dried (MgSO₄) and concentrated under reduced pressure. The residue was purified on silica gel (FC, EtOAc–hexanes, 1:3), affording 85 mg (0.28 mmol, 30% yield) of benzimidazole derivative **10** as a tan solid: mp >210 °C dec; *R*_f 0.18 (EtOAc–hexanes, 1:3); ¹H NMR (DMSO-*d*₆, 400 MHz) δ 6.39 (t, *J* = 2.2 Hz, 2H), 7.27 (br, 2H), 7.64 (br, 2H), 7.64 (t, *J* = 2.2 Hz, 2H), 7.97 (dd, *J* = 8.9, 2.5 Hz, 1H), 8.150 (d, *J* = 8.9 Hz, 1H), 8.154 (d, *J* = 2.5 Hz, 1H), 13.02 (s, 1H); MS (70 eV) *m/z* 304.1 ([*M*⁺], 100), 287.1 (83), 262.1 (23), 257 (12), 155.1 (15), 141 (15); EI–HRMS calculated for [*M*⁺] C₁₇H₁₂N₄O₂ 304.0960, found 304.1004.

c. 2-(1H-Benzimidazol-2-yl)-4-pyrrol-1-ylphenylamine (12). A solution of **10** (80 mg, 0.26 mmol) in 8 mL of ethanol was hydrogenated at atmospheric pressure in the presence of Pd on activated carbon (5 wt %, 13 mg) as catalyst. Upon completion

of the reaction (TLC) the mixture was filtered through a pad of Celite and concentrated under reduced pressure, affording 60 mg (0.22 mmol, 84% yield) of amine **12** as a tan solid: mp 163–165 °C; *R*_f 0.65 (EtOAc–hexanes, 1:2); ¹H NMR (DMSO-*d*₆, 400 MHz) δ 6.24 (t, *J* = 2.2 Hz, 2H), 6.91 (d, *J* = 8.7 Hz, 1H), 7.21–7.23 (m, 2H), 7.25 (t, *J* = 2.2 Hz, 2H), 7.37 (dd, *J* = 8.7, 2.5 Hz, 1H), 7.56–7.64 (m, br, 2H), 8.00 (d, *J* = 2.5 Hz, 1H); MS (70 eV) *m/z* 274.1 ([*M*⁺], 100), 246.1 (8), 137 (9); EI–HRMS calculated for [*M*⁺] C₁₇H₁₄N₄ 274.1219, found 274.1208.

d. {4-[2-(1H-Benzimidazol-2-yl)-4-pyrrol-1-ylphenylsulfamoyl]phenoxy}acetic Acid Ethyl Ester (4a). A solution of amine **12** (54 mg, 0.20 mmol) and ethyl (4-chlorosulfonylphenoxy)acetate¹⁶ (**14**, 66 mg, 0.24 mmol) in anhydrous pyridine (1 mL) was stirred for 2 h at room temperature. The reaction mixture was diluted with aqueous HCl (1 M, 5 mL) and extracted twice with EtOAc (10 mL). The combined organic extracts were dried with MgSO₄ and concentrated under reduced pressure. The crude product was purified on silica gel (FC, EtOAc–hexanes, 1:2), providing 45 mg (0.087 mmol, 44% yield) of **4a** as a tan solid: mp >106 °C dec; *R*_f 0.25 (EtOAc–hexanes, 1:2); ¹H NMR (CDCl₃, 400 MHz) δ 1.23 (t, *J* = 7.1 Hz, 3H), 4.17 (q, *J* = 7.1 Hz, 2H), 4.65 (s, 2H), 6.21 (d, *J* = 8.9 Hz, 2H), 6.36 (t, *J* = 2.1 Hz, 2H), 7.06–7.12 (m, 4H), 7.32–7.37 (m, 2H), 7.40–7.47 (m, 3H), 7.81 (br, 1H), 7.83 (d, *J* = 9.5 Hz, 1H), 9.98 (s, br, 1H), 11.20 (s, br, 1H); MS (70 eV) *m/z* 516.1 ([*M*⁺], 48), 273.1 (100); EI–HRMS calculated for [*M*⁺] C₂₇H₂₄N₄O₅S 516.1467, found 516.1417.

e. {4-[2-(1H-Benzimidazol-2-yl)-4-pyrrol-1-ylphenylsulfamoyl]phenoxy}acetic Acid (4b). Ester **4a** (40 mg, 0.077 mmol) was dissolved in THF (1.5 mL), and a solution of LiOH·H₂O (97 mg) in MeOH–water (1:1, 3 mL) was added. The resulting mixture was heated under reflux for 4 h and then cooled to room temperature. After removal of the organic solvent under reduced pressure, the reaction mixture was diluted with water (2 mL). Aqueous HCl (1 M) was added until the product started to precipitate. The product was filtered off, washed with little water, and dried in vacuo, affording 38 mg (0.082 mmol, 99%) of acid **4b** as a tan solid: mp >130 °C dec; *R*_f 0.44 (MeOH–CH₂Cl₂, 1:3); ¹H NMR (DMSO-*d*₆, 400 MHz) δ 4.68 (s, 2H), 6.31 (t, *J* = 2.2 Hz, 2H), 6.92 (d, *J* = 9.0 Hz, 2H), 7.33–7.37 (m, 2H), 7.41 (t, *J* = 2.2 Hz, 2H), 7.67–7.70 (m, 4H), 7.72 (br, 2H), 8.26 (s, 1H), 13.22 (br, 2H); MS (70 eV) *m/z* 488.1 ([*M*⁺], 23), 273.1 (100), 299 (79); EI–HRMS calculated for [*M*⁺] C₂₅H₂₀N₄O₅S 488.1154, found 488.1141.

f. 2-Nitro-4-pyrrol-1-yl-benzaldehyde (9). 2-Nitro-4-bromobenzaldehyde³³ (**7**, 250 mg, 1.09 mmol) was converted to pyrrole derivative **9** as described for the synthesis of **8**, yielding 102 mg (0.47 mmol, 43% yield) of **9** as a yellow solid: mp 113–115 °C; *R*_f 0.18 (EtOAc–hexanes, 1:9); ¹H NMR (CDCl₃, 400 MHz) δ 6.47 (t, *J* = 2.0 Hz, 2H), 7.22 (t, *J* = 2.0 Hz, 2H), 7.76 (dd, *J* = 8.5, 2.2 Hz, 1H), 8.07 (d, *J* = 2.2 Hz, 1H), 8.09 (d, *J* = 8.5 Hz, 1H), 10.40 (s, 1H); MS (70 eV) *m/z* 216.1 ([*M*⁺], 100), 186.1 (64), 141 (78), 130.1 (50), 115.1 (42); EI–HRMS calculated for [*M*⁺] C₁₁H₈N₂O₃ 216.0535, found 216.0544.

g. 2-(2-Nitro-4-pyrrol-1-yl-phenyl)-1H-benzimidazole (11). Aldehyde **9** (102 mg, 0.47 mmol) was converted to benzimidazole derivative **11** as described for **10**, providing 114 mg (0.37 mmol, 80% yield) of **11** as a yellow solid: mp >200 °C (dec); *R*_f 0.26 (EtOAc–hexanes, 1:2); ¹H NMR (DMSO-*d*₆, 400 MHz) δ 6.37 (t, *J* = 2.0 Hz, 2H), 7.23–7.26 (m, 2H), 7.58–7.62 (m, 2H), 7.65 (t, *J* = 2.0 Hz, 2H), 8.07 (d, *J* = 8.5 Hz, 1H), 8.13 (dd, *J* = 8.5, 2.4 Hz, 1H), 8.31 (d, *J* = 2.4 Hz, 1H), 13.06 (s,

br, 1H); MS (70 eV) m/z 304.1 ($[M^+]$, 100), 287.1 (18), 141 (15). EI–HRMS calculated for $[M^+]$ $C_{17}H_{12}N_4O_2$ 304.0960, observed 304.0937.

h. 2-(1*H*-Benzimidazol-2-yl)-5-pyrrol-1-yl-phenylamine (13). Nitrocompound **11** (110 mg, 0.36 mmol) was reduced to amine **13** as described for the synthesis of **12**, yielding 76 mg of **13** (0.28 mmol, 77% yield) as a tan solid: mp 253–255 °C; R_f 0.67 (EtOAc–hexanes, 1:1); 1H NMR (DMSO- d_6 , 400 MHz) δ 6.28 (t, J = 2.1 Hz, 2H), 6.90 (dd, J = 8.5 Hz, 2.4 Hz, 1H), 6.98 (d, J = 2.4 Hz, 1H), 7.16–7.23 (m, 2H), 7.34 (t, J = 2.1 Hz, 2H), 7.45 (s, br, 2H), 7.50 (d, br, J = 7.6 Hz, 1H), 7.64 (d, br, J = 7.6 Hz, 1H), 7.92 (d, J = 8.6 Hz, 1H), 12.69 (s, 1H); MS (70 eV) m/z 274.1 ($[M^+]$, 100), 246.1 (12); EI–HRMS calculated for $[M^+]$ $C_{17}H_{14}N_4$ 274.1219, found 274.1211.

i. {4-[2-(1*H*-Benzimidazol-2-yl)-5-pyrrol-1-yl-phenylsulfamoyl]phenoxy}acetic Acid Ethyl Ester (5a). Amine **13** (20 mg, 0.073 mmol) was reacted with ethyl (4-chlorosulfonylphenoxy)-acetate¹⁶ **14** as described above for the synthesis of **4a**, affording 25 mg (0.048 mmol, 66% yield) of **5a** as a tan solid: mp 193–195 °C; R_f 0.55 (EtOAc–hexanes, 3:2); 1H NMR (CDCl₃, 400 MHz) δ 1.30 (t, J = 7.1 Hz, 3H), 4.27 (q, J = 7.1 Hz, 2H), 4.60 (s, 2H), 6.32 (t, J = 2.1 Hz, 2H), 6.62 (d, J = 8.9 Hz, 2H), 6.88 (t, J = 2.1 Hz, 2H), 7.05 (dd, J = 8.5, 2.1 Hz, 1H), 7.18 (d, J = 2.1 Hz, 1H), 7.23–7.26 (m, 2H), 7.50 (d, J = 8.9 Hz, 2H), 7.52–7.55 (m, 2H), 7.65 (d, J = 8.6 Hz, 1H); MS (70 eV) m/z 516.1 ($[M^+]$, 28), 365.1 (9), 274.1 (100), 273 (50), 212.1 (28); EI–HRMS calculated for $[M^+]$ $C_{27}H_{24}N_4O_5S$ 516.1467, found 516.1460.

j. {4-[2-(1*H*-Benzimidazol-2-yl)-5-pyrrol-1-ylphenylsulfamoyl]phenoxy}acetic Acid (5b). Ethyl ester **5a** (10 mg, 0.019 mmol) was hydrolyzed as described for the synthesis of **4b**, yielding 10 mg (0.082 mmol, 99% yield) of acid **5b** as a tan solid: mp >190 °C (dec); R_f 0.53 (MeOH–CH₂Cl₂, 1:3); 1H NMR (DMSO- d_6 , 400 MHz) δ 4.69 (s, 2H), 6.35 (t, J = 2.1 Hz, 2H), 6.96 (d, J = 9.0 Hz, 2H), 7.31–7.37 (m, 4H), 7.51 (dd, J = 8.3, 1.6 Hz, 1H), 7.65–7.73 (m, 3H), 7.75 (d, J = 8.9 Hz, 2H), 8.13 (d, J = 8.8 Hz, 1H), 13.40 (s, br, 2H); FAB-MS (thioglycerol) m/z 489 ($[M^+]$, 13), 327 (25), 274.1 (18), 273 (17), 237 (100); EI–HRMS calculated for $[M^+]$ $C_{25}H_{21}N_4O_5S$ 489.1233, found 489.1268.

Steady-State Absorption and Fluorescence Spectroscopy.

All sample solutions were filtered through 0.45 μ m Teflon membrane filters to remove interfering dust particles or fibers. UV–vis absorption spectra were recorded at 25 °C using a Varian Cary Bio50 UV–vis spectrometer with constant-temperature accessory. Steady-state emission and excitation spectra were recorded with a PTI fluorimeter and FELIX software. For all measurements the path length was 1 cm with a cell volume of 3.0 mL. The fluorescence spectra have been corrected for the spectral response of the detection system (emission correction file provided by instrument manufacturer) and for the spectral irradiance of the excitation channel (via calibrated photodiode). Quantum yields were determined using quinine sulfate dihydrate in 0.5 M H₂SO₄ as fluorescence standard (Φ_f = 0.54 \pm 0.05).³⁴

Determination of pK_a Values. Measurements were performed with a combination glass microelectrode (Orion, Thermo Electron Corp, Waltham, MA). The electrode was calibrated for $-\log[H_3O^+]$ by titration of a standardized HCl solution (Aldrich, 0.1 N volumetric standard) with KOH (Aldrich, 0.1 N volumetric standard) at 25 °C and 0.1 M ionic strength (KCl). The end point, electrode potential, and slope were determined by Gran's method³⁵ as implemented in the software GLEE.³⁶ The calibration procedure was repeated three times prior to each

pK_a value determination. The electrode potential was measured with the Corning pH/ion analyzer 355, and the emf measurements were reproducible with \pm 0.1 mV accuracy. For the determination of the pK_a 's of a compound, a series of UV–vis spectra were acquired for which $-\log[H_3O^+]$ was varied between 3 and 10. The emf of each solution was directly measured in the quartz cell and converted to $-\log[H_3O^+]$ using E° and the slope as obtained from the electrode calibration procedure described above. The raw spectral and emf data were processed via nonlinear least-squares fit analysis using the SPECFIT software package,³⁷ providing deconvoluted spectra for each species present as well as the acidity constants for the relevant protonation equilibria.

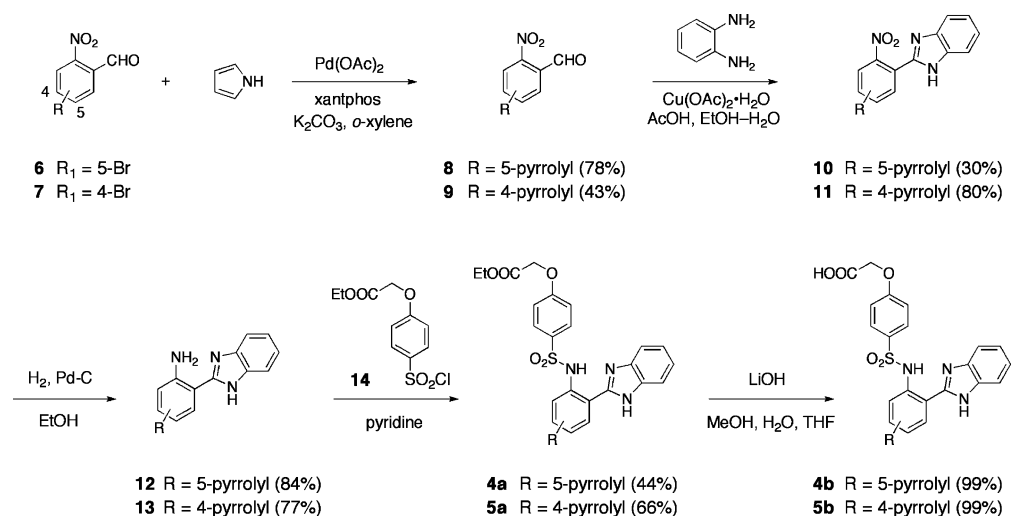
Computational Methods. Quantum chemical calculations were performed for the unsubstituted parent compound **1c** and the methoxy-substituted derivatives **2c** and **3c** using the Q-Chem³⁸ computational package. The ground state (S_0) equilibrium geometries for each compound were optimized at both ab initio Hartree–Fock (HF) and density functional theory (DFT) levels. The first excited singlet states (S_1) corresponding to the excited proton-transfer (PT) tautomers were modeled using post-HF configuration interaction including singly excited determinants (HFCIS). The diffuse 3-21+G(d,p) (3-21+G**) basis set was used in conjunction with HF methods, while the split valence polarized 6-31G(d) (6-31G*) basis set was employed with DFT considering the B3LYP hybrid exchange correlation functional.³⁹ The corresponding Hessian calculation was carried out for each optimized structure. The MOLEKEL software package⁴⁰ was used to visualize all molecular orbitals and electron attachment/detachment densities produced from Q-Chem plot data. The vertical excitation energies, state (μ) and transition (M) dipole moments, and oscillator strengths (f) were obtained using the semiempirical intermediate neglect of differential overlap (INDO) Hamiltonian⁴¹ in combination with a configuration interaction scheme including singly excited configurations (SCI) with an active space including 24 occupied and 24 unoccupied molecular orbitals, implemented in ZINDO.⁴¹ To account for extrinsic solvent effects, INDO (SCI) was combined with the self-consistent reaction field (SCRF) method⁴² for solvents methanol (MeOH) and water (H₂O) as implemented in ArgusLab.⁴³

Results and Discussion

1. Synthesis. The parent compound **1** and the two methoxy-substituted derivatives **2** and **3** were synthesized following recently published procedures.³⁰ Fluorophores **4** and **5** were obtained from the corresponding pyrrole-substituted aldehyde precursors **8** and **9**, respectively, both of which were synthesized through palladium-catalyzed amination of the corresponding bromine derivatives **6** and **7** (Scheme 1). Coupling of aldehydes **8** and **9** with 1,2-phenylenediamine using copper(II) acetate as mild oxidant yielded the corresponding benzimidazole derivatives **10** and **11**, respectively. After palladium-catalyzed hydrogenation of the nitro group at ambient pressure, the resulting amines **12** and **13** were reacted with sulfonyl chloride¹⁶ **14** to give the desired sulfonamide substituted fluorophores **4a** and **5a**, respectively. While the ester derivatives **1a–5a** were suitable for solvatochromic shift studies in organic solvents, their solubility was insufficient for aqueous solution experiments. For the latter purpose, the corresponding acid derivatives **1b–5b** were used which were obtained by hydrolysis of the ethyl esters **1a–5b** with lithium hydroxide in methanol–water.

2. Protonation Equilibria. Deprotonation of the sulfonamide nitrogen in 2-(2'-arylsulfonamidophenyl)benzimidazole derivatives results in a strong bathochromic shift of the lowest energy

SCHEME 1



absorption band.^{16,28} A comparison of the absorption spectra of fluorophores **1a–5a** is therefore only meaningful if the spectra represent a well-defined protonation state. We determined therefore the UV–vis traces for the fully deprotonated species L^{2–} and the monoprotonated species LH[–] from a series of pH titrations by means of spectral deconvolution, which at the same time also yielded the pK_a value of the sulfonamide nitrogen for each derivative. The corresponding deconvoluted spectra for each fluorophore are shown in Figure 1 (left), and a compilation of the protonation constants together with selected photophysical data for the deprotonated and monoprotonated species is given in Table 1.

The measured pK_a values of the sulfonamide nitrogen range between 7.3 and 8.3, and depend strongly on the attachment position of the donor-substituent (Table 1). Compared to the parent compound **1b**, substitution with a methoxy-group in the *para*-position to the sulfonamide group raised the pK_a by 0.3 units (compound **2b**), while substitution in the *meta*-position lowered it by 0.4 units (compound **3b**).³⁰ The observed differences follow closely the expectation based on the interplay between resonance stabilization and inductive effects. While for the *para*-substituted derivative **2b**, the electron-donating resonance contribution outweighs the inductive effect imposed through the electronegative oxygen, the reverse situation is present for the *meta*-substituted compound **3b**. Similarly, the sulfonamide group of the *para*-substituted pyrrole derivative **4b** is less acidic compared to its *meta*-substituted analog **5b**; however, both pK_a's are significantly lower compared to the unsubstituted parent compound **1b**. These data indicate that the pyrrole group acts in the ground state primarily as a σ -accepting substituent with a stronger electron-withdrawing inductive component compared to the π -donating resonance contribution.

3. Absorption and Fluorescence Spectra in Aqueous Solution. UV–Vis Spectra. According to previous studies, the photophysical properties of 2-(2'-arylsulfonamidophenyl)benzimidazole fluorophores are significantly influenced by donor or acceptor substituents attached to the fluorophore π -system.³⁰ While the deconvoluted absorption spectra corresponding to the monoprotonated species LH[–] showed only small changes for the methoxy-substituted fluorophores **2b** and **3b** compared to the parent compound **1b** (Figure 1a–c, left, solid traces), the pyrrole-substituted derivative **4b** revealed a substantially different spectrum indicating significant electronic interactions between the pyrrole-ring and the fluorophore π -system (Figure 1d, left). In contrast, derivative **5b** containing the pyrrole-ring

in the *meta*-position relative to the sulfonamide group showed a UV–vis spectrum that is, with the exception of overall red-shifted bands, qualitatively very similar compared to the spectrum of the analogous methoxy-substituted fluorophore **3b**. Interestingly, both *meta*-substituted derivatives **3b** and **5b** revealed an additional low-energy band centered around 360–370 nm (Figure 1, parts c and e, left). On basis of photophysical studies on structurally related 2-(2'-hydroxyphenyl)benzimidazole derivatives^{15,44} this band originates most likely from a prototropic tautomer that is already present in the ground state equilibrium (vide infra). The fully deprotonated species L^{2–} showed for all derivatives **1b–5b** a substantially red-shifted absorption maximum compared to the monoprotonated species LH[–] (Figure 1a–e, left, dashed traces). The bathochromic shift was strongest for the pyrrole-substituted fluorophore **4b** and **5b**, followed by the 5-methoxy-substituted derivative **2b**, while the spectrum of the 4-methoxy-substituted derivative **3b** revealed no significant changes compared to the parent compound **1b**.

Fluorescence Spectra. While attachment of a methoxy-substituent to the central benzene ring resulted only in minor changes of the absorption spectra, the fluorescence emission maxima were altered significantly compared to the unsubstituted parent compound **1b** (Figure 1, right). When excited at 300 nm, all derivatives **1b–5b** showed a single emission band with large Stokes shifts ranging between 9120 to 13 430 cm^{–1} (Table 1). Upon deprotonation of the sulfonamide nitrogen at high pH, the fluorescence maxima of all derivatives were shifted by more than 2000 cm^{–1} to higher energy, indicating disruption of the ESIPT process that was responsible for the large Stokes shifted emission band at neutral pH. Notably, none of the derivatives exhibited dual emission,³⁰ suggesting that formation of the ESIPT tautomer is very efficient and compromised by neither solvent hydrogen-bonding interactions⁴⁵ nor ground-state stabilization of a rotamer that cannot undergo ESIPT.^{15,44} Further inspection of the emission energy trends revealed a surprising difference. While for the 5-methoxy-substituted derivative **2b** the fluorescence emission of the ESIPT tautomer appears at lower energy by 1620 cm^{–1} compared to the parent compound **1b** (Figure 1b), the 4-methoxy-substituted derivative **3b** showed a hypsochromic shift by 1145 cm^{–1} (Figure 1c). As apparent from the data in Table 1, the observed shifts of the tautomer emission energies are primarily an expression of changes in Stokes shifts, thus indicating significant differences in the relaxation energetics of the initially formed Franck–Condon state. It is conceivable that the opposing shifts might be a result

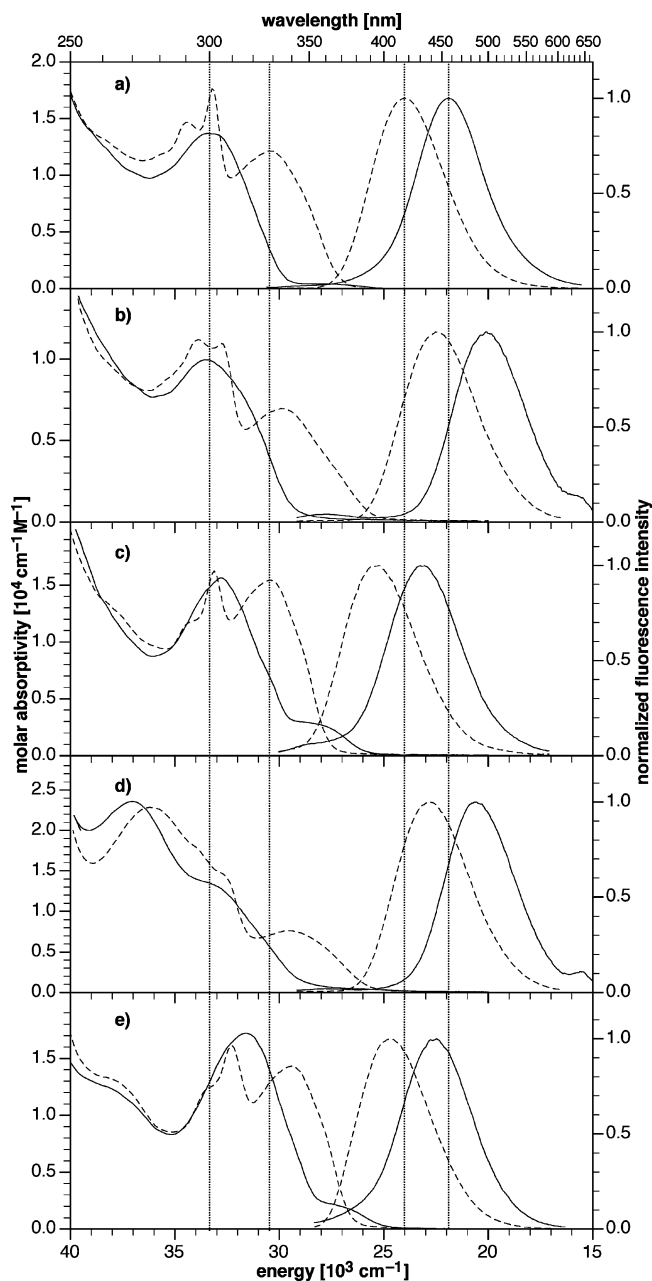


Figure 1. Deconvoluted UV-vis absorption spectra (left) and normalized fluorescence emission spectra (right) of fluorophore: (a) **1b**, (b) **2b**, (c) **3b**, (d) **4b**, and (e) **5b** in aqueous solution (0.1 M KCl, 25 °C). UV-vis traces for the species with protonated (—) and deprotonated (---) sulfonamide group were obtained through deconvolution of a series of spectra with pH ranging between 6 and 10. The emission spectra were directly recorded at pH 6.0 (—) and 11.0 (---) without deconvolution analysis (excitation at the isosbestic point).

of different solvation modes of the methoxy substituent. Naturally, the methoxy group would be expected to adopt a coplanar conformation with regard to the benzene ring. Such a conformation benefits from resonance stabilization through π -donation of the oxygen lone-pair electrons, while at the same time still offering a nonbonding orbital for H-bonding interactions with the solvent. However, H-bonding interactions with the second lone-pair of oxygen might outweigh the resonance stabilization, particularly in a strongly H-bonding solvent such as water. Consequently, the methoxy substituent would be rotated out-of-plane, thus acting as a σ -accepting rather than π -donating group. If conformational differences mediated through H-bonding interactions with the methoxy lone-pair

electrons were to play a key role in dictating the tautomer emission energy, we would expect a significantly different behavior for the pyrrole-substituted compounds **4b** and **5b**. In these derivatives, the *N*-pyrrolyl-substituent can still act as a π -donor, but the nitrogen lone-pair is now an integral part of the aromatic heterocycle rendering H-bonding induced conformational changes energetically highly unfavorable. As is evident from Figure 1, parts d and e (right), the pyrrole-substituted derivatives revealed qualitatively the same trends as observed for the methoxy-substituted fluorophores **2b** and **3b**, namely an increased emission energy for the 4-substituted derivative **5b**, and a decreased energy for the 5-substituted derivative **4b**. Hence, it is unlikely that conformational differences through H-bonding interactions with the methoxy-group are responsible for the opposing emission energy shifts.

Ground-State Tautomer Equilibrium. To further clarify the nature of the low-energy absorption band that is observed for derivative **3b** but absent in **2b**, we acquired the fluorescence emission spectra of **3b** in aqueous solution at $-\log[\text{H}_3\text{O}^+] = 6.0$ covering a broad excitation energy range between 26 000–40 000 cm^{-1} . At this proton concentration, the fraction of monoprotonated species LH^- vs fully deprotonated L^{2-} is greater than 97%. A contour plot of the emission intensities revealed a symmetrical profile with a single emission maximum centered at 437 nm (22 883 cm^{-1}) throughout the entire excitation energy range (Figure 2a), suggesting that only one emitting species is formed regardless of the excitation energy. Normalized individual slices of the contour plot at various excitation energies are identical within experimental error and further support the presence of a single species undergoing excited-state radiative deactivation (Figure 2b). If the low-energy absorption band were due to the presence of ground-state rotamers that cannot undergo ESIPT, excitation into this band should yield emission with a normal Stokes shift at significantly higher energy. The absence of such a high-energy band together with the uniform nature of the emission profile suggests that the monoprotonated species LH^- is engaged in a ground-state equilibrium between the protonated sulfonamide and its prototropic imino tautomer, which is usually only formed through intramolecular proton transfer upon photoexcitation. Excitation into the low-energy absorption band thus yields the same emissive species as formed through ESIPT at higher excitation energies. Quantum chemical calculation additionally confirmed that the ground-state imino tautomer is more effectively stabilized by attaching a donor-substituent in the 4- rather than 5-position of the central benzene ring (see section 5.1).

The surprisingly divergent dependence of the emission energy on the donor-attachment position may be simply a reflection of an increased or decreased excited-state polarization. Particularly in polar solvents such as water, variations in dipole moment differences between ground and excited states would be expected to significantly alter the corresponding Stokes shifts. Alternatively, the divergent emission energy trends could originate from a solvent-independent effect. For example, the attachment position of the donor substituent might differentially stabilize excited vs ground state of the emissive ESIPT tautomer, thus leading to large variations in the Stokes shifts. To explore the first possibility we performed a systematic solvatochromic shift analysis, while the latter scenario was investigated by quantum chemical calculations (vide infra).

4. Solvatochromic Shift Studies. Solvatochromism is a direct consequence of solvent-solute interactions, either through specific, anisotropic interactions of the fluorophore with solvent molecules in the first solvation shell, or through nonspecific,

TABLE 1: Protonation Constants and Photophysical Data of Benzimidazole Derivatives 1b–5b in Aqueous Solution^a

| species | data | 1b ^b | 2b | 3b | 4b | 5b |
|------------------|--|-----------------|-------------|-------------|-------------|-------------|
| pK _{a1} | [L ²⁻][H ⁺]/[LH ⁻] | 8.04 ± 0.03 | 8.34 ± 0.02 | 7.60 ± 0.01 | 7.69 ± 0.01 | 7.28 ± 0.01 |
| pK _{a2} | [LH ⁻][H ⁺]/[LH ₂] | 4.50 ± 0.04 | 4.54 ± 0.05 | 4.79 ± 0.01 | 4.32 ± 0.05 | 4.44 ± 0.02 |
| L ²⁻ | absorption ^[c] λ _{max} (nm) | 301 (1.59) | 305 (1.10) | 302 (1.62) | 277 (2.28) | 310 (1.61) |
| | | 329 (1.09) | 334 (0.70) | 329 (1.54) | 339 (0.76) | 340 (1.43) |
| | excitation ^[d] λ _{max} (nm) | 296 | 297 | 330 | 337 (sh) | 310 |
| | emission ^[d] λ _{max} (nm) | 418 | 444 | 396 | 438 | 404 |
| | quantum yield ^[e] | 0.26 | 0.27 | 0.06 | 0.32 | 0.32 |
| | Stokes shift (cm ⁻¹) | 6470 | 7420 | 5140 | 6660 | 4660 |
| LH ⁻ | absorption ^[c] λ _{max} (nm) | 299 (1.23) | 298 (1.00) | 305 (1.57) | 270 (2.36) | 316 (1.72) |
| | | | | | 303 (sh) | |
| | excitation λ _{max} (nm) | 300 | 295 | 308 | n/a | 321 |
| | emission λ _{max} (nm) | 460 | 497 | 437 | 485 | 444 |
| | Stokes shift (cm ⁻¹) | 11 700 | 13 430 | 9640 | 12 380 | 9120 |
| | quantum yield ^[e] | 0.23 | 0.14 | 0.17 | 0.16 | 0.13 |
| LH ₂ | absorption ^[c] λ _{max} (nm) | 290 (1.31) | 292 (1.07) | 303 (1.69) | 272 (2.35) | 316 (1.79) |

^a 0.1 M KCl, 25 °C. ^b Data from ref 16. ^c From deconvolution analysis, molar extinction coefficient [10⁴ L mol⁻¹ cm⁻¹] in parentheses. ^d pH 11.20, 0.1 M KCl. ^e Quinine sulfate in 1 N H₂SO₄ as standard.

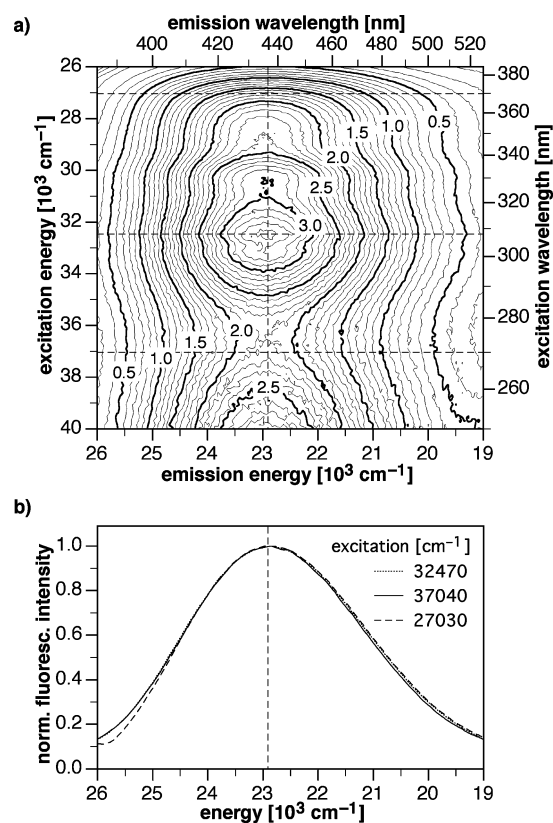


Figure 2. Fluorescence emission profiles for fluorophore **3b** (0.1 M KCl, $-\log[\text{H}_3\text{O}^+] = 6.0$). (a) Two-dimensional fluorescence contour plot showing the emission profile as a function of excitation energy. (b) Normalized emission spectra for selected emission energies.

isotropic interactions in which the solvent is assumed to act as dielectric continuum.⁴⁶ The complexity of intermolecular solvent–solute interactions has led to the development of numerous theories as well as empirical approaches to interpret the solvatochromic shift behavior of a molecule. Such analyses can provide significant insights into the role of dipole–dipole interactions, H-bonding, and other intermolecular interactions in the ground and excited states of a fluorophore.

For the following solvatochromic shift studies, the UV–vis and fluorescence emission spectra of each fluorophore were acquired in a set of 15 solvents. To avoid artifacts caused by partial dissociation of the carboxylic acid moiety in polar solvents, the experiments were carried out with the ethyl ester derivatives **1a**, **2a**, **3a**, **4a**, and **5a** rather than the carboxylic

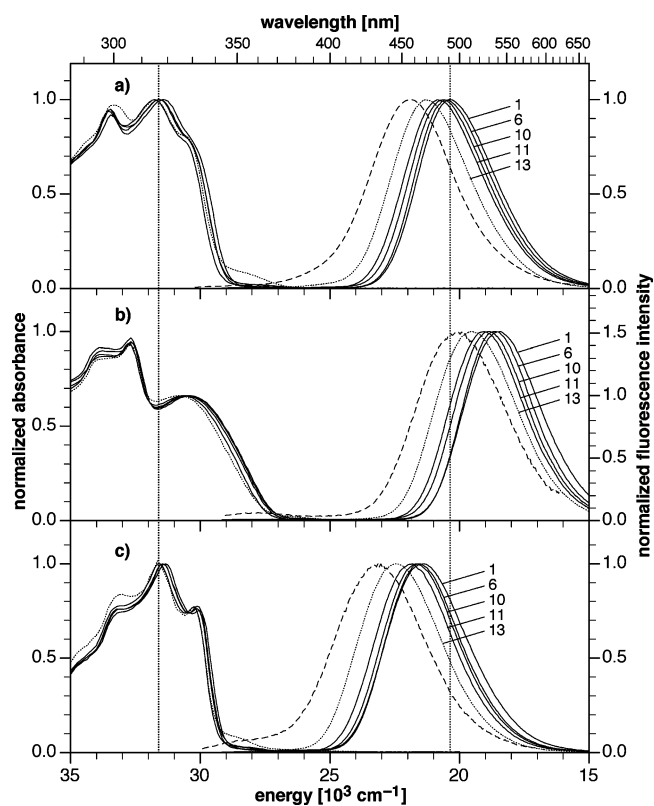


Figure 3. Normalized UV–vis absorption (left) and fluorescence excitation at peak absorption energy) for derivatives (a) **1a**, (b) **2a**, and (c) **3a**, in selected organic solvents illustrating the solvatochromic shift behavior (solvent legend : no. 1 1,4-dioxane, no. 6 ethylacetate, no. 10 butyronitrile, no. 11 acetonitrile, no. 13 ethanol). For comparison, the fluorescence emission spectra of the water-soluble compounds **1b**, **2b**, and **3b** in aqueous buffer (pH 6.0, 0.1 M KCl) have been also included (dashed traces).

acids used for the photophysical studies in aqueous solution. A compilation of all peak energies is given in Tables S2–S6 provided with the Supporting Information. To illustrate the trends in solvatochromic shift behavior, Figure 3 shows the normalized absorption and fluorescence emission spectra of the methoxy-substituted compounds **2a** and **3a** compared to the unsubstituted parent compound **1a** in a few representative solvents.

As is evident from Figure 3 (left), the various solvents have only little effect on the appearance and peak energies in the UV–vis absorption spectra, revealing overall a slight increase

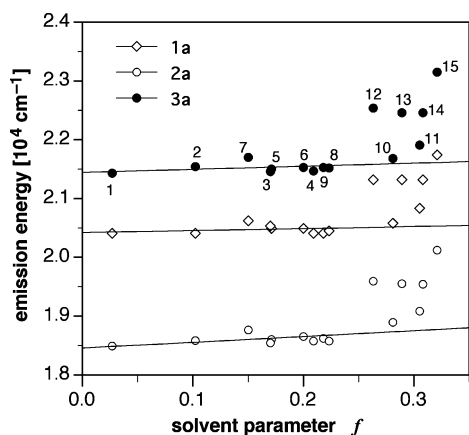


Figure 4. Correlation of the peak emission energies of derivative **1a**, **2a**, and **3a** with the solvent polarity parameter $f(\epsilon, n)$. The plotted linear regression line does not include acetonitrile (no. 11) and any protic solvents (nos. 12–15). The solvent numbering scheme and values for $f(\epsilon, n)$ are given in Table S1 provided with the Supporting Information.

in energy with increased solvent polarity. The observed, small negative solvatochromic shifts suggest a slightly decreased dipole moment in the Franck–Condon excited-state compared to the ground state for all three compounds. The differences in the peak fluorescence emission energies are slightly more pronounced, exhibiting also negative solvatochromic shifts for all three fluorophores. It is worthwhile mentioning that protic solvents appear to induce a stronger blue shift than would be expected solely based on their polarity. For example, for all three derivatives, the emission energy in ethanol is higher by more than 500 cm^{-1} compared to butyronitrile, despite the fact that both solvents have nearly identical dielectric permittivities of 24.55 and 24.56, respectively.

To further explore and quantify differences between the three derivatives regarding the importance of H-bonding vs dipole–dipole interactions on the Stokes shifts and emission energies, we analyzed the solvatochromic shift data by means of Onsager’s reaction field model,⁴⁷ Reichardt’s empirical solvent polarity scale $E_T(30)$,⁴⁶ as well as Kamlet–Taft’s empirical solvent index.⁴⁸

Onsager’s Reaction Field Model. In this model, the solute is considered to be located in a cavity of defined size and its permanent dipole moment is responsible for polarization of surrounding solvent molecules, which in turn gives rise to a field that electrostatically interacts with the solute, thus leading to a net stabilization.⁴⁷ If the solute dipole moment is altered upon excitation, the ground and excited states are differently stabilized which leads to the solvatochromic shift behavior. In general, fluorophores with large dipole moment changes between ground and excited-state exhibit also a strong solvatochromism. Hence, if isotropic electrostatic solute–solvent interactions are the primary source of the observed solvatochromism, the Stokes shift, absorption, or emission energy should correlate linearly with the solvent polarity parameter $f(\epsilon, n)$ according to eq 1⁴⁹

$$\nu = m f(\epsilon, n) + \text{constant} \quad (1)$$

with

$$f(\epsilon, n) = \frac{\epsilon - 1}{2\epsilon + 1} - \frac{n^2 - 1}{2n^2 + 1}$$

A plot of the peak emission energy vs the solvent polarity parameter $f(\epsilon, n)$ is shown in Figure 4 for fluorophores **1a**, **2a**,

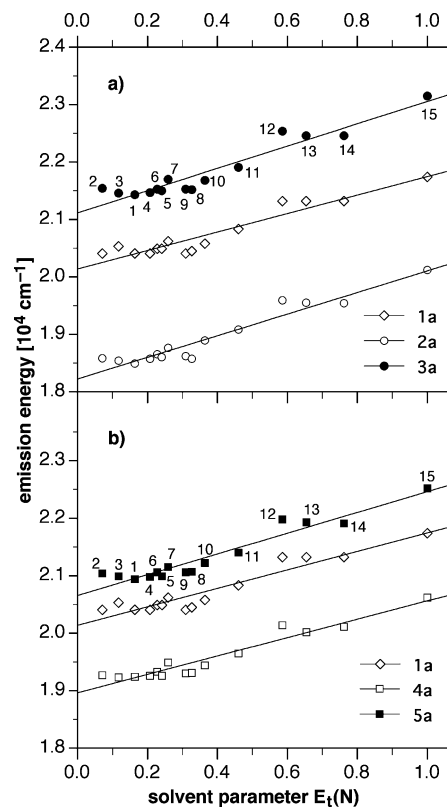


Figure 5. Linear regression analysis of the solvatochromic emission shifts according to Reichardt’s $E_T(30)$ empirical solvent polarity scale. (a) Linear correlation of the peak emission energies of the methoxy-substituted compounds **2a** and **3a**. (b) Linear correlation for compounds **4a** and **5a**. For ease of comparison, the data for the unsubstituted parent compound **1a** are included in both graphs.

and **3a**. Linear regression analysis reveals a good correlation for all non-protic solvents, while the emission energy is significantly offset in H-bond donating solvents such as butanol, ethanol, methanol, or water (solvent nos. 12–15). This behavior is independent of the position of the methoxy-substituent attached to the central benzene ring. In fact, all three derivatives **1a–3a** exhibit similarly flat slopes in Figure 4, suggesting only small and uniform changes in the dipole moments between excited and ground states. From this analysis, we can conclude that the observed divergent dependence of the emission energy on the donor-attachment position cannot be explained in terms of variations in dipole moment differences $\Delta\mu$ between excited and ground states of the emissive phototautomer.

Reichardt’s $E_T(30)$ Solvent Scale. This empirical solvent polarity scale is based on the negative solvatochromism of a pyridinium *N*-phenolate betaine dye as a probe molecule, and is particularly useful for the analysis of the solvent dependence of UV–vis absorption and emission energies.⁴⁶ Although solvatochromic shift correlations with solvent parameters based on a single molecule probe are inherently limited to reveal solute–solvent interactions that are specific to the probe, such correlations benefit from the fact that the properties of the reference system are well understood and clearly defined. For example, the basic character of the betaine dye probe is known to cause more pronounced shifts in H-bond donor solvents. As a consequence, Reichardt’s $E_T(30)$ polarity scale includes specific solvent acidity effects.⁴⁶ As is evident from Figure 5 and Table 2, the solvatochromic shifts of the peak emission energies of all five fluorophores **1a–5a** correlate well with the $E_T(30)$ solvent polarity scale. Even the emission energies measured for the corresponding water-soluble derivatives **1b–**

TABLE 2: Fitted Parameters for the Regression Analysis of the Solvatochromic Peak Fluorescence Emission Shifts According to the $E_T(30)$ Empirical Solvent Model^a

| parameter | 1a | 2a | 3a | 4a | 5a |
|--|--------------|-------------|--------------|--------------|--------------|
| slope [cm ⁻¹] ^b | 1605 (±148) | 1882 (±147) | 1941 (±166) | 1597 (±127) | 1803 (±145) |
| intercept [cm ⁻¹] ^b | 20 140 (±68) | 18222 (±68) | 21 114 (±76) | 18 966 (±58) | 20 658 (±67) |
| correlation coeff | 0.949 | 0.962 | 0.956 | 0.961 | 0.960 |

^a Linear regression includes all 15 solvents listed in Table S1. ^b Standard deviation in parentheses.

TABLE 3: Fitted Parameters for the Multiple Regression Analysis of the Solvatochromic Peak Fluorescence Emission Shifts According to the Kamlet–Abboud–Taft Empirical Solvent Model

| parameter | 1a | 2a | 3a | 4a | 5a |
|---|--------------|--------------|--------------|--------------|--------------|
| dielectric interactions (<i>s</i> , [cm ⁻¹]) | 369 (±198) | 580 (±262) | 386 (±208) | 304 (±182) | 388 (±212) |
| H-bonding donor (<i>a</i> , [cm ⁻¹]) | 842 (±91) | 910 (±121) | 977 (±96) | 824 (±84) | 904 (±98) |
| H-bonding acceptor (<i>b</i> , [cm ⁻¹]) | 224 (±199) | 540 (±263) | 322 (±209) | 349 (±183) | 330 (±214) |
| ν_0 [cm ⁻¹] | 20221 (±163) | 18131 (±216) | 21215 (±171) | 19010 (±150) | 20727 (±175) |
| correlation coeff <i>r</i> | 0.976 | 0.968 | 0.980 | 0.977 | 0.976 |

5b (solvent no. 15) in aqueous buffer agree well with an overall linear fit. As also observed for the correlation with Onsager's reaction field model, the slope of the linear regression is very similar for all five derivatives, indicating similar strengths of the solute–solvent interactions regardless of the nature of the substituent on the central benzene ring. In contrast, the intercept for both 4-substituted derivatives (**3** and **5**) is shifted to higher energy compared to the parent compound **1**, while the 5-substituted derivatives **2** and **4** are shifted to lower energy. This observation further supports our earlier conclusion that the divergent emission behavior between the 4- and 5-methoxy-substituted derivatives is not caused through specific or non-specific solvent interactions but must be routed in differences of their respective electronic structures (vide infra). In addition, the excellent correlation with Reichardt's empirical solvent polarity scale unequivocally confirms the importance of H-bond donor solvent–solute interactions for understanding the observed solvatochromism.

Kamlet–Abboud–Taft's solvent index (KAT).⁴⁸ The solvatochromic shift analysis according to Onsager's model demonstrated the importance of anisotropic interactions for this fluorophore class; however, it did not provide any information to quantify these interactions relative to nonspecific dielectric contributions. Kamlet and Taft proposed a multiple linear regression approach that can be used to correlate a set of solvatochromic shift data with additional solvent-dependent parameters. According to this model the UV–vis absorption or emission energies are fitted to three (or more) solvent-specific indices π^* , α , and β according to eq 2:

$$\nu = \nu_0 + s\pi^* + a\alpha + b\beta \quad (2)$$

where ν_0 refers to the absorption or emission energy in vacuum, and *s*, *a*, and *b* are the corresponding fitted parameters obtained from a multiple linear regression analysis. Comparable to Onsager's reaction field model, the index π^* is a measure for the dipolarity and polarizability of a solvent, thus expressing the ability to stabilize a solute charge or dipole through nonspecific dielectric interactions. The indices α and β describe the solvent's ability to act as hydrogen bond donor and acceptor, respectively. A comprehensive list of the 3 indices for each of the 15 solvents used in this study is given in Table S1 (Supporting Information).⁵⁰

Multiple regression analysis of the solvatochromic shift data of all five fluorophores **1a–5a** yielded excellent correlation coefficients (Table 3). A comparison of the three fitted parameters *s*, *a*, and *b* indicates that the solvent's hydrogen bonding donor strength is the dominant contribution to the

solvatochromic emission shifts of all five derivatives. In agreement with the Onsager reaction field analysis, the polarizability parameter *s* is relatively small and remains within experimental error almost identical across all five derivatives. Furthermore, the gas-phase emission energies ν_0 correlate qualitatively well with the trends in Stokes shifts, further corroborating the previous conclusion that solute–solvent interactions do not play a key role in explaining the peculiar donor-substituent effects on the emission energies.

5. Quantum Chemical Calculations. In order to investigate whether the observed dependence of the emission shifts on the substituent position correlates with the intrinsic electronic properties of the excited proton-transfer tautomer, we performed a series of quantum chemical calculations. The observed emission shifts were more pronounced for the methoxy- than the pyrrole-substituted compounds; therefore, the computational studies focused exclusively on the 4- and 5-methoxy-substituted fluorophores and the unsubstituted parent compound as a reference. To further reduce computational costs, the pendent carboxymethyl-substituents (OCH₂–COOR') were replaced with methoxy groups (OCH₃) yielding the corresponding model compounds **1c**, **2c**, and **3c** (Chart 1). Variation of the substituent at the tosyl ring had a negligible effect on the resulting geometries or transition energies for which deviations were on the order of <0.05 eV (data not shown).

5.1. Structural Studies. The geometries of the neutral ground states (*S*₀) of the three model compounds **1c**, **2c**, and **3c** were optimized at the HF/3-21+G(d,p) and DFT-B3LYP/6-31G(d) levels, followed by a vibrational frequency analysis to ensure a stationary point, although zero point vibrational energy corrections were not applied. Given the limited range of theories for which excited-state analytical gradients are available, the structures of the corresponding excited proton-transfer (PT) tautomers were determined only at the HFCIS/3-21+G(d,p) level of theory. The 3-21+G(d,p) basis set has been shown to adequately reproduce excited-state geometries with only minor differences compared to larger basis sets such as 6-31G*.^{51,52}

Ground-State Geometry. Given the considerable size of the molecules, we first determined the least expensive model chemistry that would adequately reproduce the molecular structures and photophysical properties compared to experimental data. The structure of the unsubstituted parent compound had been formerly characterized by means of X-ray crystallography,²⁸ and thus served as a reference to gauge the quality of the applied theoretical models. Geometry optimizations were carried out at the DFT-B3LYP/6-31G(d) and HF/3-21+G(d,p) levels of theory. While both methods yielded similar ground

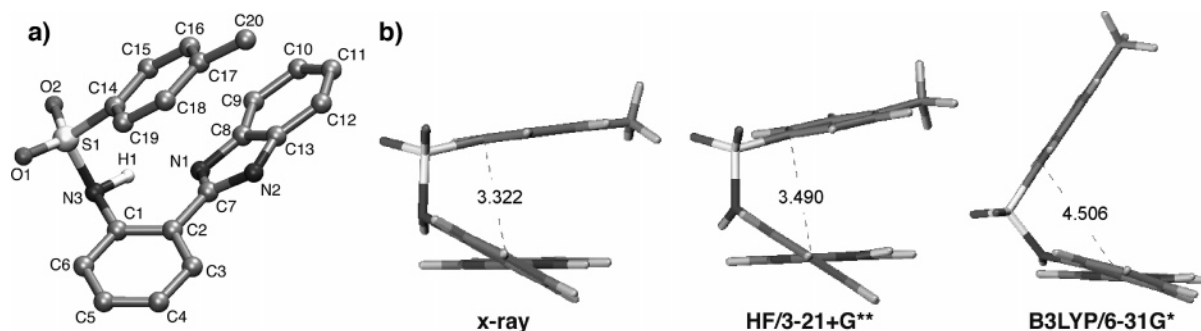


Figure 6. (a) X-ray structure of 2-(2'-tosylaminophenyl)-benzimidazole (TPBI)²⁸ with numbering scheme (hydrogen atoms are omitted for clarity). (b) Projection along C2–C7 for the experimental structure (left) and the geometry optimized structures at the HF/3-21+G(d,p) (center) and B3LYP/6-31G(d) (right) levels of theory. The labels indicate interatomic distances (Å) between the tosyl and imidazole planes.

TABLE 4: Selected Geometric Parameters of 2-(2'-Tosylaminophenyl)-benzimidazole (TPBI) from Optimizations at Different Levels of Theory in Comparison to the Experimental X-ray Crystal Structure (Numbering Scheme Shown in Figure 6a)

| parameter | X-ray | B3LYP/6-31G(d) | HF/3-21+G(d,p) | HF/6-31+G(d,p) |
|-------------------|-------|----------------|----------------|----------------|
| C1–C2–C7–N1 (deg) | –28.6 | –14.3 | –34.6 | –29.6 |
| C2–C1–N3–S1 (deg) | –99.3 | –135.2 | –104.0 | –119.5 |
| C14–S1–N3 (deg) | 106.6 | 106.2 | 105.0 | 107.1 |
| S1–N3–C1 (deg) | 116.1 | 124.7 | 121.5 | 123.2 |
| C2–C7 (Å) | 1.465 | 1.465 | 1.467 | 1.478 |
| C1–N3 (Å) | 1.444 | 1.408 | 1.433 | 1.415 |
| S1–N3 (Å) | 1.647 | 1.695 | 1.632 | 1.646 |
| S1–C14 (Å) | 1.751 | 1.795 | 1.755 | 1.770 |
| C1–C2 (Å) | 1.397 | 1.424 | 1.396 | 1.402 |

TABLE 5: Selected Geometric Parameters for the 4- and 5-Methoxy-Substituted Benzimidazole Derivatives 2c and 3c in Comparison to the Unsubstituted Parent Compound 1c, All Optimized at the HF/3-21+G(d,p) Level (Numbering Scheme Shown in Figure 6a)

| parameter | 1c | 2c | 3c |
|----------------------|--------|--------|--------|
| C1–C2–C7–N1 (deg) | –34.6 | –36.2 | –34.4 |
| C2–C1–N3–S1 (deg) | –104.0 | –102.9 | –104.4 |
| C14–S1–N3 (deg) | 105.0 | 105.3 | 104.8 |
| S1–N3–C1 (deg) | 121.5 | 121.5 | 121.8 |
| C2–C7 (Å) | 1.467 | 1.467 | 1.464 |
| S1–N3 (Å) | 1.632 | 1.630 | 1.632 |
| C1–C2 (Å) | 1.396 | 1.388 | 1.403 |
| C1–C6 (Å) | 1.385 | 1.391 | 1.375 |
| C5–C6 (Å) | 1.385 | 1.376 | 1.389 |
| C4–C5 (Å) | 1.387 | 1.390 | 1.384 |
| C3–C4 (Å) | 1.383 | 1.380 | 1.387 |
| C2–C3 (Å) | 1.391 | 1.397 | 1.385 |
| aryl C–methoxy O (Å) | n/a | 1.378 | 1.374 |

state geometries in terms of bond lengths and angles, significant differences were observed for some of the dihedral angles (Table 4). As is evident from projections along the interannular C2–C7 bond (Figure 6), the HF/3-21+G(d,p) optimized geometry closely resembles that of the X-ray structure, while the DFT-B3LYP/6-31G(d) geometry displays significant deviations. The experimental structure is characterized by a nearly parallel orientation of the tosyl and benzimidazole ring planes with a separation of ~ 3.3 Å, indicating significant intramolecular π -stacking interactions. Consequently, the benzimidazole moiety is considerably twisted out-of-plane as reflected by the dihedral angle (C1–C2–C7–N1) of -28.6° . HF/3-21+G(d,p) not only preserves the parallel π -stacking orientation along with a similar twist angle (-34.6°), but also performs slightly better than DFT-B3LYP/6-31G(d) in terms of reproducing the experimental bond lengths and bond angles (Table 4). Interestingly, the parallel face-to-face orientation is entirely absent in the DFT geometry. The resulting geometry possesses a smaller out-of-plane twist of the benzimidazole moiety of -14.4° , approximately half the value as in the experimental structure (Table 4).

The HF/3-21+G(d,p) optimized geometry reproduced well the key structural features of the experimental structure. To gain further confidence in this model, we also explored to what extent a higher-level HF optimization with larger basis set might improve the geometry. As is evident from Table 4, the structure optimized at the HF/6-31+G(d,p) (6-31+G**) level exhibits only minor changes compared to HF/3-21+G(d,p). The most noteworthy improvement of the HF/6-31+G(d,p) geometry lies in the out-of-plane twist of the benzimidazole moiety. The interannular dihedral angle C1–C2–C7–N1 of -29.6° compares very favorably with the experimental value of -28.6° ; however, beyond this parameter there were no significant advantages of using the larger basis set over HF/3-21+G(d,p). Furthermore, with the exception of the S1–N3 bond most interatomic distances were better modeled using the smaller 3-21+G(d,p) basis set in comparison to the X-ray structure. A comprehensive list of all computational data pertaining to the geometry-optimized structures at various levels of theory, including atomic coordinates and energies, is provided with the Supporting Information.

Given the success of HF/3-21+G(d,p) in reproducing the experimental molecular geometry, we restricted the quantum chemical studies of the methoxy-substituted compounds **2c** and **3c** to the HF/3-21+G(d,p) and HFCIS/3-21+G(d,p) optimized geometries. As is evident from Table 5, the HF/3-21+G(d,p) geometries of the 5- and 4-methoxy-substituted derivatives **2c** and **3c** are very similar compared to the unsubstituted parent compound **1c**. Notably, both structures display the face-to-face orientation of the tosyl and benzimidazole moieties observed in the X-ray crystal structure and the HF/3-21+G(d,p) geometry of the unsubstituted parent compound. When compared to the geometry of the unsubstituted parent compound **1c**, the molecular structures of the methoxy-substituted derivatives **2c** and **3c** revealed small but significant differences that can be ascribed to differences in degree of electron delocalization. For example, the interannular C2–C7 bond is slightly shorter for the 4-methoxy-substituted derivative **3c** compared to 5-substituted **2c**, resulting also in a slightly more acute interannular dihedral

TABLE 6: Selected Geometric Parameters for the Energy-Minimized Lowest Excited Singlet State of the 4- and 5-Methoxy-Substituted Benzimidazole Derivatives 2c and 3c and the Parent Compound 1c, All Optimized at the HFCIS/3-21+G(d,p) Level (Numbering Scheme Shown in Figure 6a)

| parameter | 1c | 2c | 3c |
|----------------------|--------|--------|--------|
| C1–C2–C7–N1 (deg) | −0.2 | −0.3 | −0.5 |
| C2–C1–N3–S1 (deg) | −174.1 | −173.5 | −173.3 |
| C14–S1–N3 (deg) | 103.2 | 103.4 | 102.9 |
| S1–N3–C1 (deg) | 129.4 | 129.2 | 129.2 |
| N3–C1–C2 (deg) | 114.0 | 114.4 | 113.9 |
| C2–C7 (Å) | 1.402 | 1.405 | 1.401 |
| C1–N3 (Å) | 1.330 | 1.334 | 1.328 |
| C7–N1 (Å) | 1.370 | 1.368 | 1.373 |
| S1–N3 (Å) | 1.615 | 1.610 | 1.617 |
| C1–C2 (Å) | 1.490 | 1.484 | 1.492 |
| C1–C6 (Å) | 1.407 | 1.407 | 1.401 |
| C5–C6 (Å) | 1.387 | 1.380 | 1.385 |
| C4–C5 (Å) | 1.397 | 1.399 | 1.392 |
| C3–C4 (Å) | 1.393 | 1.394 | 1.392 |
| C2–C3 (Å) | 1.401 | 1.400 | 1.401 |
| aryl C–methoxy O (Å) | n/a | 1.367 | 1.382 |

angle C1–C2–C7–N1 for **3c**. Likewise, the bonds C1–C6 and C3–C4 are shorter in **3c** compared to **2c**, indicating a significant degree of π -delocalization of the methoxy oxygen lone pair across the central benzene ring toward the benzimidazole moiety. This trend of divergent π -bond alternation between the two methoxy-substituted derivatives can be observed across all bond lengths listed in Table 5, where shorter bonds in one derivative are elongated in the other system while the corresponding values of the unsubstituted parent compound lie in between. The increased π -electron delocalization in the 4-methoxy derivative **3c** is also reflected in the energetics of the geometry optimized structures: the additional resonance stabilization renders the *meta*-substituted derivative **3c** more stable by 0.02 eV (~ 1.7 kJ mol^{−1}) compared to **2c**.

Excited-State Geometry. The geometries of the lowest excited singlet state (*S*₁) of the corresponding phototautomers of **1c**, **2c**, and **3c** were each optimized at the HFCIS/3-21+G(d,p) level of theory. In all cases, the geometry optimization converged at a saddle point of the excited-state potential surfaces as indicated by the presence of imaginary vibrational modes. A more detailed analysis revealed that these modes correspond to torsional deformations of the central benzene ring and the benzimidazole heterocycle. Sobolewski et al. reported a similar phenomenon in association with 2-(2'-hydroxyphenyl)benzotriazoles, for which the constrained optimized excited proton-transfer tautomer represents a "pseudo-minimum" resting in a shallow well of the potential surface.^{53–55} Any attempts to employ commonly used techniques to remove the imaginary frequencies were unsuccessful at this level of theory; however, given the success of our model in reproducing the essential photophysical trends (*vide infra*), we are confident that the computed excited-state structures are representative of the emissive states of these compounds. Table 6 summarizes selected features of the excited-state geometries in the unsubstituted parent compound **1c** and the two methoxy-substituted derivatives **2c** and **3c**.

The most noticeable difference between the *S*₁ and ground state geometries is the planarization of the central aryl and benzimidazole rings for which the interannular dihedral angle (C1–C2–C7–N1) approaches 0°. In conjunction with this flattening of the excited-state structure is the loss of the parallel face-to-face orientation of the terminal benzenesulfonyl and benzimidazole rings. This can be best seen in the large opening of the C2–C1–N3–S1 dihedral angle from −104° in the ground state to approximately −174° in the excited state, thus

TABLE 7: Experimental and Calculated Vertical Excitation and Emission Energies (eV) for 1c–3c

| parameter | 1c | 2c | 3c |
|---|-------|-------|-------|
| Excitation [eV] | | | |
| INDO–SCI | 4.12 | 4.11 | 4.09 |
| <i>f</i> ^a | 0.355 | 0.360 | 0.492 |
| <i>M</i> _{ge} [D] ^b | 4.8 | 4.8 | 5.6 |
| expt ^c | 4.13 | 4.20 | 4.07 |
| Emission [eV] | | | |
| INDO–SCI | 2.61 | 2.52 | 2.66 |
| <i>f</i> ^a | 0.447 | 0.462 | 0.429 |
| <i>M</i> _{ge} [D] ^b | 6.7 | 6.9 | 6.5 |
| expt ^c | 2.70 | 2.49 | 2.84 |
| gas-phase fit ^d | 2.51 | 2.25 | 2.63 |

^a Oscillator strength. ^b Transition dipole moment. ^c Measured in aqueous solution, 0.1 M ionic strength (KCl). ^d Extrapolated gas-phase values from Kamlet–Abboud–Taft empirical solvent model.

TABLE 8: HFCIS/3-21+G(d,p)/INDO–SCI Computed Ground and Excited State Dipole Moments and Their Differences for 1c–3c

| parameter | 1c | 2c | 3c |
|-----------------------|------|------|------|
| Gas Phase | | | |
| μ_g [D] | 13.4 | 14.4 | 15.2 |
| μ_e [D] | 11.1 | 12.8 | 12.7 |
| $\mu\Delta$ [D] | −2.2 | −1.6 | −2.5 |
| Solution Phase (MeOH) | | | |
| μ_g [D] | 15.6 | 16.9 | 17.4 |
| μ_e [D] | 13.2 | 15.0 | 15.1 |
| $\mu\Delta$ [D] | −2.4 | −1.9 | −2.4 |

resulting in an essentially perpendicular orientation of the benzenesulfonyl and benzimidazole ring planes in all three derivatives. The twisting of the benzenesulfonyl moiety in the *S*₁ structure is accompanied by a decrease in the N3–C1–C2 bond angle which positions N3 in closer proximity to H1, thus facilitating a fast back transfer of the proton in the ground state. There are also significant differences noticeable in the C–C bond lengths of the central aryl ring when comparing the *S*₁ and *S*₀ geometries. For example, in the ground state of the parent compound **1c**, the C–C bond distances of the central benzene ring are nearly equivalent, which is consistent with a fully delocalized aromatic ring system. In contrast, the corresponding C–C bonds in the excited-state geometry resemble more a quinoidal structure with increased double bond character for C5–C6 and increased single bond character for C1–C6 and C2–C3. Likewise, the methoxy-substituted derivatives **2c** and **3c** exhibit similar excited-state geometry distortions. In agreement with the quinoidal nature of the excited photo tautomer, the interannular C2–C7 bond is shortened for all three derivatives by approximately 0.06 Å compared to the ground state geometry.

5.2. Photophysical Properties. To acquire a qualitative understanding of the photophysical properties of the unsubstituted parent compound and its 4- and 5-methoxy-substituted derivatives (**1c–3c**), the vertical transition energies, corresponding to *S*₀–*S*₁ absorption and *S*₁–*S*₀ fluorescence, were computed using configuration interaction including only singly excited determinants (SCI) as implemented in ZINDO with the INDO Hamiltonian. The INDO–SCI scheme has been shown to be computationally efficient and reliable for many different types of compounds.⁵⁶ A compilation of the computational data including oscillator strengths, state dipole moments, and transition dipole moments for **1c–3c** is given in Tables 7 and 8.

Absorption Spectra. In agreement with the experimental data, the INDO–SCI gas-phase vertical transition energies for the lowest excited singlet states show only slight differences among

the three derivatives **1c**–**3c** (Table 7). When the calculations included a SCRF solvent model that corrected for the dielectric constant of methanol, the transition energies were lowered by less than 0.1 eV while preserving the overall trend (Supporting Information). It is noteworthy that the calculated transition energy of 4.07 eV for the lowest excited singlet state of **3c** is consistent with the energy of the main absorption band with a maximum at 305 nm (4.07 eV). The quantum chemical calculations thus further support our interpretation that the weak low-energy absorption band in the UV–vis spectrum of **3c** (Figure 1c) does not originate from the normal cis-ground-state species. To investigate whether the low-energy band might arise from the proposed imino tautomer, we optimized the ground state geometry for this structure at the HF/3-21+G(d,p) level followed by an INDO–SCI calculation. On the basis of these data, the lowest energy absorption of the imino tautomer was indeed predicted to occur at significantly lower energy (3.0 eV) compared to the cis-ground-state species (4.09 eV). A dual Gaussian curve fit of the low-energy portion of the absorption spectrum yielded a peak energy of 3.45 eV for the low-energy band. Although the deviation of 0.45 eV between theory and experiment is somewhat larger than for the normal ground-state species, the calculations reproduce well the relative trends in peak energies between the two tautomers and further support the proposed structural assignment.

Emission Spectra. The fluorescence peak energies were predicted on the basis of the vertical excitation energies of the geometry-optimized excited-state structures for each of the corresponding phototautomers. In contrast to the absorption energies, we found that the donor position had a profound effect on the transition energies for emission of the excited-state proton-transfer species (Table 7). The experimental trends in the spectral shifts are reproduced well by the computations, which predicted for **2c** a lower energy emission compared to parent compound **1c** and a higher energy emission for **3c**. When considering methanol as the dielectric isotropic solvent environment with an SCRF model, the emission energies increased for all compounds, an observation consistent with the observed negative solvatochromism. A more detailed analysis of the excited-state polarization of the proton-transfer species revealed that in all cases the excited-state dipole moment μ_e is smaller than the ground state dipole moment μ_g ; this again is consistent with the negative solvatochromic behavior displayed by each compound (Table 8). Donor substitution led to an increase in both μ_g and μ_e with respect to the parent compound, however, without rendering $\Delta\mu = \mu_e - \mu_g$ distinctly different from **1c**. Interestingly, the excited-state dipole moments of both methoxy-substituted derivatives were calculated to be very similar in the gas phase and in methanol. Hence, these data strongly indicate that the observed spectral shifts upon donor substitution cannot be simply attributed to differences in reorganization due to the degree of excited-state polarization.

To further elucidate the mechanism responsible for the changes in transition energies upon donor substitution, we analyzed the nature of the excited phototautomer of each derivative **1c**–**3c** by means of an electron attachment and detachment density analysis.⁵⁷ The attachment/detachment densities reflect the electron redistribution upon excitation, and therefore can help in locating that portion of the molecular wave function involved in the S_1 – S_0 transition most affected by donor substitution. Since the S_1 – S_0 transition is dominated by the HOMO–LUMO configuration (for a full CI-description, see Supporting Information), the attachment/detachment densities closely resemble the densities associated with the HOMO and

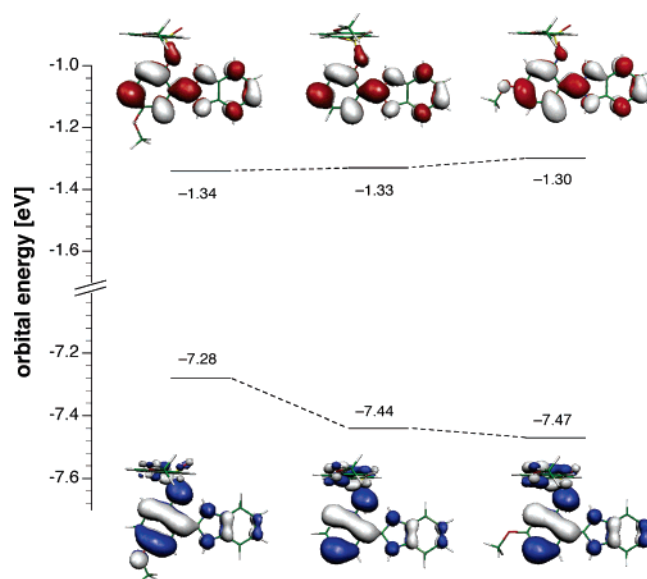


Figure 7. Energy level diagram for the frontier orbitals of the phototautomer of compounds **1c**–**3c**. A plot of the HOMO and LUMO isosurfaces is also depicted for each compound.

LUMO for each compound. Hence, we restricted our analysis to a discussion of the HOMO and LUMO wave functions themselves. Figure 7 shows the HOMO and LUMO energies of the phototautomer for each compound as well as the corresponding orbital isodensity surfaces. The changes in the electronic structure that depend on the donor position can be readily rationalized by examining the nodal structure of the wave functions.⁵⁸ In compound **1c**, the carbon atom at position 5 of the central benzene ring contributes strongly to the HOMO, but only weakly to the LUMO; the opposite is true for the carbon atom in position 4, which is hardly involved in the HOMO but strongly contributing to the LUMO. Upon attachment of a methoxy-group in the 5-position (compound **2c**), the HOMO energy is significantly increased while the LUMO energy remains almost unaffected. This can be readily rationalized by inspecting the corresponding orbital densities, which reveal a large coefficient on C5 for the HOMO but a very small coefficient (node) for the LUMO. As a consequence, the HOMO–LUMO gap significantly decreases which translates into a red-shifted emission energy for **2c** compared to **1c**. Conversely, the LUMO of **3c** is slightly destabilized with respect to the parent compound **1c**, while its HOMO energy remains virtually unchanged. As a result, the peak emission of **3c** is shifted to higher energy, in full accordance with the experimental data.

Conclusions

Combined photophysical and quantum chemical studies provided significant insights into the origin of the substituent-dependent fluorescence properties of this class of ESIPT fluorophores. Solvatochromic shift analysis based on several solvent theories demonstrated that the ESIPT tautomers emit from a moderately polarized excited-state whose dipole moment is not strongly influenced by the donor-attachment position. The negative solvatochromic behavior was most pronounced in protic solvents due to specific hydrogen-bonding interactions. Given the fact that the pyrrole derivatives **4** and **5** showed qualitatively the same behavior as their methoxy-substituted counter parts, hydrogen bonding with the methoxy-oxygen lone pairs in compounds **2** and **3** does not appear to be a critical factor in altering the fluorescence energy. However, the extrapolated

vacuum emission energies obtained from the solvatochromic analyses varied strongly as a function of the donor substituent and its attachment position on the central benzene ring. Conclusively, the divergent emission energy shift must be due to differences in the HOMO–LUMO gap of the various derivatives. Detailed quantum chemical calculations not only confirmed the moderately polarized nature of the ESIPT tautomer, but also provided a rationale for the observed substituent position dependent emission shifts. In summary, the results gained from this study should provide guidelines for fine-tuning of the emission properties of this class of ESIPT fluorophores, which might find applications in analytical chemistry, biochemistry, or materials science.

Acknowledgment. Financial support by the National Institutes of Health (DK68096) is gratefully acknowledged. Computations were supported by the Center for Computational Molecular Science and Technology at the Georgia Institute of Technology and under National Science Foundation CRIF Award CHE-0443564. We thank Dr. Egbert Zoer for helpful discussions, and David Bostwick for mass spectral data.

Supporting Information Available: Tables of spectroscopic absorption and fluorescence emission data for compounds **1a**–**5a** in selected solvents and a tabular summary of all computational results, including Cartesian atomic coordinates of geometry optimized structures and all computed photophysical parameters. This material is available free of charge via the Internet at <http://pubs.acs.org>.

References and Notes

- (1) Cardoso, M. B.; Samios, D.; da Silveira, N. P.; Rodembusch, F. S.; Stefani, V. *Photochem. Photobiol. Sci.* **2007**, *6*, 99–102.
- (2) Rodembusch, F. S.; Leusin, F. P.; Medina, L. F. D.; Brandelli, A.; Stefani, V. *Photochem. Photobiol. Sci.* **2005**, *4*, 254–259.
- (3) Holler, M. G.; Campo, L. F.; Brandelli, A.; Stefani, V. *J. Photochem. Photobiol. A* **2002**, *149*, 217–225.
- (4) Tanaka, K.; Kumagai, T.; Aoki, H.; Deguchi, M.; Iwata, S. *J. Org. Chem.* **2001**, *66*, 7328–7333.
- (5) Klymchenko, A. S.; Stoeckel, H.; Takeda, K.; Mely, Y. *J. Phys. Chem. B* **2006**, *110*, 13624–13632.
- (6) Klymchenko, A. S.; Duportail, G.; Mely, Y.; Demchenko, A. P. *Proc. Natl. Acad. Sci. U.S.A.* **2003**, *100*, 11219–11224.
- (7) Shynkar, V. V.; Klymchenko, A. S.; Duportail, G.; Demchenko, A. P.; Mely, Y. *Biochim. Biophys. Acta. Biomembr.* **2005**, *1712*, 128–136.
- (8) Garcia-Ochoa, I.; Lopez, M. A. D.; Vinas, M. H.; Santos, L.; Ataz, E. M.; Amat-Guerri, F.; Douhal, A. *Chem.—Eur. J.* **1999**, *5*, 897–901.
- (9) Mateo, C. R.; Douhal, A. *Proc. Natl. Acad. Sci. U.S.A.* **1998**, *95*, 7245–7250.
- (10) Klymchenko, A. S.; Demchenko, A. P. *J. Am. Chem. Soc.* **2002**, *124*, 12372–12379.
- (11) Klymchenko, A. S.; Duportail, G.; Ozturk, T.; Pivovarenko, V. G.; Mely, Y.; Demchenko, A. P. *Chem. Biol.* **2002**, *9*, 1199–1208.
- (12) Klymchenko, A. S.; Mely, Y.; Demchenko, A. P.; Duportail, G. *Biochim. Biophys. Acta-Biomembr.* **2004**, *1665*, 6–19.
- (13) Huang, J.; Peng, A. D.; Fu, H. B.; Ma, Y.; Zhai, T. Y.; Yao, J. N. *J. Phys. Chem. A* **2006**, *110*, 9079–9083.
- (14) Wu, Y. K.; Peng, X. J.; Fan, J. L.; Gao, S.; Tian, M. Z.; Zhao, J. Z.; Sun, S. *J. Org. Chem.* **2007**, *72*, 62–70.
- (15) Henary, M. M.; Fahrni, C. J. *J. Phys. Chem. A* **2002**, *106*, 5210–5220.
- (16) Henary, M. M.; Wu, Y. G.; Fahrni, C. J. *Chem.—Eur. J.* **2004**, *10*, 3015–3025.
- (17) Taki, M.; Welford, J. L.; O'Halloran, T. V. *J. Am. Chem. Soc.* **2004**, *126*, 712–713.
- (18) Ohshima, A.; Momotake, A.; Arai, T. *Tetrahedron Lett.* **2004**, *45*, 9377–9381.
- (19) Qin, W.; Obare, S. O.; Murphy, C. J.; Angel, S. M. *Analyst* **2001**, *126*, 1499–1501.
- (20) Roshal, A. D.; Grigorovich, A. V.; Doroshenko, A. O.; Pivovarenko, V. G.; Demchenko, A. P. *J. Phys. Chem. A* **1998**, *102*, 5907–5914.
- (21) Douhal, A.; Roshal, A. D.; Organero, J. A. *Chem. Phys. Lett.* **2003**, *381*, 519–525.
- (22) Zhang, X. B.; Peng, J.; He, C. L.; Shen, G. L.; Yu, R. Q. *Anal. Chim. Acta* **2006**, *567*, 189–195.
- (23) Chattopadhyay, N.; Mallick, A.; Sengupta, S. *J. Photochem. Photobiol. A* **2006**, *177*, 55–60.
- (24) Abou-Zied, O. K.; Jimenez, R.; Thompson, E. H. Z.; Millar, D. P.; Romesberg, F. E. *J. Phys. Chem. A* **2002**, *106*, 3665–3672.
- (25) Barbara, P. F.; Brus, L. E.; Rentzepis, P. M. *J. Am. Chem. Soc.* **1980**, *102*, 5631–5.
- (26) Das, K.; Sarkar, N.; Majumdar, D.; Bhattacharyya, K. *Chem. Phys. Lett.* **1992**, *198*, 443–8.
- (27) Douhal, A.; Amat-Guerri, F.; Lillo, M. P.; Acuna, A. U. *J. Photochem. Photobiol. A* **1994**, *78*, 127–38.
- (28) Fahrni, C. J.; Henary, M. M.; Van Derveer, D. G. *J. Phys. Chem. A* **2002**, *106*, 7655–7663.
- (29) Lochbrunner, S.; Wurzer, A. J.; Riedle, E. *J. Phys. Chem. A* **2003**, *107*, 10580–10590.
- (30) Henary, M. M.; Wu, Y. G.; Cody, J.; Sumalekshmy, S.; Li, J.; Mandal, S.; Fahrni, C. J. *J. Org. Chem.* **2007**, in press.
- (31) Rodembusch, F. S.; Leusin, F. P.; Campo, L. F.; Stefani, V. *J. Lumin.* **2006**, doi:10.1016/j.jlumin.2006.11.007.
- (32) Jung, M. E.; Dansereau, S. M. K. *Heterocycles* **1994**, *39*, 767–78.
- (33) Hu, Y.-Z.; Zhang, G.; Thummel, R. P. *Org. Lett.* **2003**, *5*, 2251–2253.
- (34) Demas, J. N.; Crosby, G. A. *J. Phys. Chem.* **1971**, *75*, 991–1024.
- (35) Gran, G. *Analyst* **1951**, *77*, 661.
- (36) Gans, P.; O'Sullivan, B. *Talanta* **2000**, *51*, 33–37.
- (37) Binstead, R. A.; Zuberbühler, A. D.; SPECFIT v. 3.0.27. Spectrum Software Associates, Marlborough MA, 2001.
- (38) Kong, J.; White, C. A.; Krylov, A. I.; Sherrill, D.; Adamson, R. D.; Furlani, T. R.; Lee, M. S.; Lee, A. M.; Gwaltney, S. R.; Adams, T. R.; Ochsenfeld, C.; Gilbert, A. T. B.; Kedziora, G. S.; Rassolov, V. A.; Maurice, D. R.; Nair, N.; Shao, Y. H.; Besley, N. A.; Maslen, P. E.; Dombroski, J. P.; Daschel, H.; Zhang, W. M.; Korambath, P. P.; Baker, J.; Byrd, E. F. C.; Van Voorhis, T.; Oumi, M.; Hirata, S.; Hsu, C. P.; Ishikawa, N.; Florian, J.; Warshel, A.; Johnson, B. G.; Gill, P. M. W.; Head-Gordon, M.; Pople, J. A. *J. Comput. Chem.* **2000**, *21*, 1532–1548.
- (39) Becke, A. D. *J. Chem. Phys.* **1993**, *98*, 5648–5652.
- (40) Flückiger, P.; Lüthi, H. P.; Portmann, S.; Weber, J.; MOLEKEL, v. 4.1. Swiss Center for Scientific Computing, Manno, 2000–2001.
- (41) Ridley, J.; Zerner, M. *Theor. Chim. Acta* **1973**, *32*, 111–134.
- (42) Karelson, M. M.; Zerner, M. C. *J. Phys. Chem.* **1992**, *96*, 6949–6957.
- (43) Thompson, M. A.; ARGUSLAB, Planaria Software LLC, Seattle, WA, <http://www.arguslab.com:2003>.
- (44) Mosquera, M.; Penedo, J. C.; Rodriguez, M. C. R.; Rodriguez-Prieto, F. *J. Phys. Chem.* **1996**, *100*, 5398–5407.
- (45) Penedo, J. C.; Mosquera, M.; Rodriguez-Prieto, F. *J. Phys. Chem. A* **2000**, *104*, 7429–7441.
- (46) Reichardt, C. *Chem. Rev.* **1994**, *94*, 2319–2358.
- (47) Onsager, L. *J. Am. Chem. Soc.* **1936**, *58*, 1486–1493.
- (48) Kamlet, M. J.; Abboud, J. L.; Taft, R. W. *J. Am. Chem. Soc.* **1977**, *99*, 6027–6038.
- (49) Lippert, E. Z. *Elektrochem.* **1957**, *61*, 962–975.
- (50) Kamlet, M. J.; Abboud, J. L. M.; Abraham, M. H.; Taft, R. W. *J. Org. Chem.* **1983**, *48*, 2877–2887.
- (51) Gao, H. Z.; Su, Z. M.; Qin, C. S.; Mo, R. G.; Kan, Y. H. *Int. J. Quantum Chem.* **2004**, *97*, 992–1001.
- (52) Halls, M. D.; Schlegel, H. B. *Chem. Mater.* **2001**, *13*, 2632–2640.
- (53) Flom, S. R.; Barbara, P. F. *Chem. Phys. Lett.* **1983**, *94*, 488–493.
- (54) Otterstedt, J. A. *J. Chem. Phys.* **1973**, *58*, 5716–5725.
- (55) Sobolewski, A. L.; Domcke, W.; Hättig, C. *J. Phys. Chem. A* **2006**, *110*, 6301–6306.
- (56) Fabian, J. *Theor. Chem. Acc.* **2001**, *106*, 199–217.
- (57) Head-Gordon, M.; Grana, A. M.; Maurice, D.; White, C. A. *J. Phys. Chem.* **1995**, *99*, 14261–14270.
- (58) Avilov, I.; Marsal, P.; Brédas, J. L.; Beljonne, D. *Adv. Mater.* **2004**, *16*, 1624–1629.